Hydrodynamics and gas-liquid mass transfer around a confined sliding bubble

Abderrahmane Kherbeche, Mei Mei, Marie-Jean Thoraval, Gilles Hébrard, Nicolas Dietrich

To cite this version:

Abderrahmane Kherbeche, Mei Mei, Marie-Jean Thoraval, Gilles Hébrard, Nicolas Dietrich. Hydrodynamics and gas-liquid mass transfer around a confined sliding bubble. Chemical Engineering Journal, 2020, 386, 10.1016/j.cej.2019.04.041 . hal-02158081

HAL Id: hal-02158081
https://insa-toulouse.hal.science/hal-02158081v1

Submitted on 17 Jun 2019

HYDRODYNAMICS AND GAS-LIQUID MASS TRANSFER AROUND A CONFINED SLIDING BUBBLE

Abderrahmane Kherbeche[1,*], Mei Mei[2,3], Marie-Jean Thoraval[1], Gilles Hébrard[2] and Nicolas Dietrich[2]

[1] State Key Laboratory for Strength and Vibration of Mechanical Structures, Shaanxi Key Laboratory of Environment and Control for Flight Vehicle, International Center for Applied Mechanics, School of Aerospace, Xi'an Jiaotong University, Xi'an 710049, P. R. China

[2] Laboratoire d'Ingénierie des Systèmes Biologiques et des Procédés (LISBP), Université de Toulouse, CNRS, INRA, INSA, Toulouse, France

[3] Laboratoire de Génie Chimique LGC, Université de Toulouse, CNRS, INPT, UPS, Toulouse, France

*Corresponding author: Abderrahmane Kherbeche

E-mail: akherbeche@xjtu.edu.cn

Abstract

An experimental investigation of gas-liquid mass transfer in the wake of a confined air bubble sliding under an inclined wall in a 2D Hele-Shaw cell is reported. A colorimetric technique based on an oxygen-sensitive dye was used to visualize the oxygen transfer. Bubble velocities, shape eccentricities, interfacial areas and, for the first time, the instantaneous spatio-temporal distribution of oxygen concentration fields in the bubble wake, have been investigated for upper wall inclination angles of $10° \leq \alpha \leq 60°$ and Archimedes numbers of $783 \leq Ar \leq 3221$. Image processing has allowed, through a specific approach, a quantification of mass transfer. The calculation of the mass flux allowed the deduction of the liquid-side mass transfer coefficient k_L. Experiments reveals that, at low angles of inclination, bubble velocities decelerates, shape eccentricities increased, and the instantaneous spatial and temporal distribution of oxygen concentration fields illustrated two distinct regions underneath the sliding bubble: a single vortex loop enclosing the near wake where oxygen is transferred, and a far wake containing oxygen in the form of a single long strip. When inclination angles and bubble sizes were increasing, velocities were increasing, the vortex elongated gradually until it disappears at high angles where total mass fluxes increased. This increase of bubble velocities has increased liquid-side mass transfer coefficient k_L allowing a scaling law between the Sherwood number and the modified Archimedes number $Ar.sin(\alpha)$ to be proposed.

Keywords: Gas/Liquid/Solid reactors, Sliding bubble; Visualization; Hydrodynamics; Mass transfer coefficient.

1. Introduction

Gas/liquid/solid contactors are crucial for processes that require high efficiencies of gas-liquid mass transfer [1–3]. They have many applications in chemical and environmental engineering, e.g., water and wastewater treatment, hydrogenations, fluorinations, and biochemical reactions, among others. The confinement of bubbles (gas phase) in constricted geometries may be a key to enhancing the performance of existing gas/liquid/solid GLS reactors such as trickle beds, bio-filters, slurry bubble columns, or large scale batch reactors [4–6]. It has several proven advantages, such as:

i. reducing gas-liquid mass transfer resistance, since the global volumetric gas-liquid mass transfer coefficient $k_L.a$ is 2 to 7 times greater in confined structures than in large turbulent contactors [4,6];
ii. extending bubble residence time inside the reactor [7–10];
iii. enlarging the average gas-liquid surface area so that more area is available for mass transfer [6,11,12];
iv. limiting gas-liquid mass transfer dissipation [6,13];
v. enhancing the transfer efficiency in the thin liquid film between bubbles and the confining solid structures [6];
vi. improving the compactness of industrial gas/liquid/solid reactors [4,6].

It is well known that local investigations are fundamental to understand gas-liquid mass transfer mechanisms. However, to the best of our knowledge, no research has been reported on the local visualization and characterization of gas-liquid mass transfer around confined ‘sliding’ bubbles, even though they could significantly improve the mass transfer in GLS reactors.

In general, confined rising bubbles, or bubbles rising in a thin gap between parallel plates, differ from freely rising bubbles in that inertia is predominant. Therefore, their behavior has some features that could alter their dynamics and shapes [7,8,16,17]. Liquid films are thinned between the bubble and the solid surfaces during the confinement, while the bubble shape deformations are amplified with fewer degrees of freedom, and its wakes are affected by shear stress at the boundaries of the solid surface [8,17].

Depending on the confinement factor $f= w/d_b$, where d_b and w are the equivalent diameter of the bubble and the thickness of the cell, respectively, confined bubbles are slightly slower compared to the unconfined, but their behavior and wake structure remain comparable [8]. In addition, their hydrodynamic regimes have been found similar to those of freely rising bubbles, (spherical, ellipsoidal or spherical cap) and their succession depends on the Archimedes number [7,14,17–19]. This non-dimensional number controls the confined bubble dynamics.

In the ellipsoidal regime ($500 < Ar < 6000$), it has been found that the bubble wake exhibits vortex shedding with two-dimensional vortices released at the bubble rears [8], in which dissolved oxygen usually deposits immediately after gas-liquid mass transfer [6,20–24].

Roudet et al., [6] revealed the important contribution of bubble confinement to the increase in gas-liquid mass transfer by comparing the results of confined bubbles in a Hele-Shaw cell and their equivalent free ones. The transferred mass was higher and even amplified from larger confined bubbles. For example, for a confined bubble of diameter 3 cm, the oxygen mass transfer rate was about twice that of a free bubble of the same volume (8.8×10^{-6} g/s as compared to 4.1×10^{-6}g/s) [6]. Furthermore, it was found that liquid films, located between the bubble surface and the Hele-Shaw cell plates, were the dominant contributor (~87%) to the gas-liquid mass transfer [25].

By changing from rising bubbles to sliding ones, Maxworthy [9] performed one of the first studies of the dynamics of a bubble sliding under an inclined surface, explaining that sliding bubbles differed from free rising bubbles in that they only experienced a predominant buoyancy force [9,26–29]. Depending on the angle of inclination of the upper wall and the bubble size, several behaviors of bubbles can be found: (i) bouncing for low angles of $\alpha < 5°$ [29], (ii) sliding for intermediate angles $5° < \alpha < 80°$ [26,27,30], or (iii) steady bouncing of constant amplitude for high angles [18,31]).

Recently, sliding bubble dynamics (d_b = 5.76 ± 0.15 mm and 7.23 ± 0.08 mm) and their flow structure in quiescent water have been investigated by combining high-speed imaging and Particle Image Velocimetry PIV under three different angles of inclination (α=20°, 30°, and 40°) [26–28]. It has been shown that an increase of α and bubble d_b increased the bubble velocities [9,30,32]. In addition, the spatial and temporal evolution of the flow structures consisted of two distinct regions: (i) a near wake moving in close association with the bubble, forming a recirculation region after which fluid separated from this high-velocity region and was drawn towards the inclined surface. (ii) A far wake, where fluid moved away from the surface in an asymmetrical shape, corresponding to oppositely oriented tails of hairpin vortices at a greater distance from the bubble [28,33].

However, there is a surprising lack of literature concerning gas-liquid mass transfer studies around sliding bubbles, for which there are important research questions that need to be solved. In fact, in the case of confined 'sliding' bubbles, the velocity of bubbles is expected to decrease with decreasing angles of inclination of the upper wall. In all the theories describing interfacial gas-liquid mass transfer (the film model, penetration theory and the surface renewal model), decreasing velocity will lead to a linear decrease in the liquid-side mass transfer coefficient k_L [34,35]. However, it is still unknown how transferred oxygen will grow underneath sliding bubbles. Local experimental investigations and effective local visualization allowing accurate quantification of the gas-liquid mass transfer are required.

Therefore, this study will elucidate the effects of inclination angles and bubble sizes on gas-liquid mass transfer around sliding bubbles in order to provide further explanations of the mass transfer mechanisms involved. In order to quantify mass transfer around the confined sliding bubbles, a visualization technique based on a colorimetric method coupled with high-speed imaging was performed. This technique, developed by Dietrich et al., [36] and experimented by Kherbeche et al., [13]; Yang et al., [12]; and Kovats et al., [37] allows clear visualization of oxygen concentrations and an accurate gas-liquid mass transfer quantification.

2. Materials and methods

2.1. The Hele-Shaw cell

The experimental setup consisted of a transparent Hele-Shaw cell (200 × 100 × 3 mm) made of PMMA (PolyMethylMethAcrylate), designed to allow 2D visualization of gas-liquid mass transfer (Figure 1b). The cell, placed on an inclinable support, was packed with thin walls made of polyvinyl chloride (PVC). They had the same width as the thickness of the cell. They were cut using water pressure and were mounted inside at in-plane inclination angles, α, of 10°, 15°, 30°, 45° and 60° to the horizontal 0° (Figure 1a). Angles were measured using a Bosch® inclinometer accurate to within 0.1°. The liquid was introduced slowly from the top of the cell. A drain tap was fitted at the bottom of the cell to evacuate the liquid easily after each experiment. The cell was carefully washed between two experiments.

The air bubble injection system was composed of three thin glass capillaries producing confined bubbles with equivalent diameters ranging from 4 to 11 mm. This system was connected by silicone rubber tubing to an automatically controlled syringe (Harvard Apparatus PHD 2000) that enabled high repeatability of the released bubble sizes. This repeatability is higher from 4 mm < d_b < 7 mm. The syringe was filled with air, and the flow rate was chosen to produce only a single repeatable bubble at a time. Released confined bubbles rises for the same height (1 cm) and impact at the same position at the right of the inclined wall, and then slid under it (Figure 1a) for total distances of 70 mm from right to left in the vertical cell.

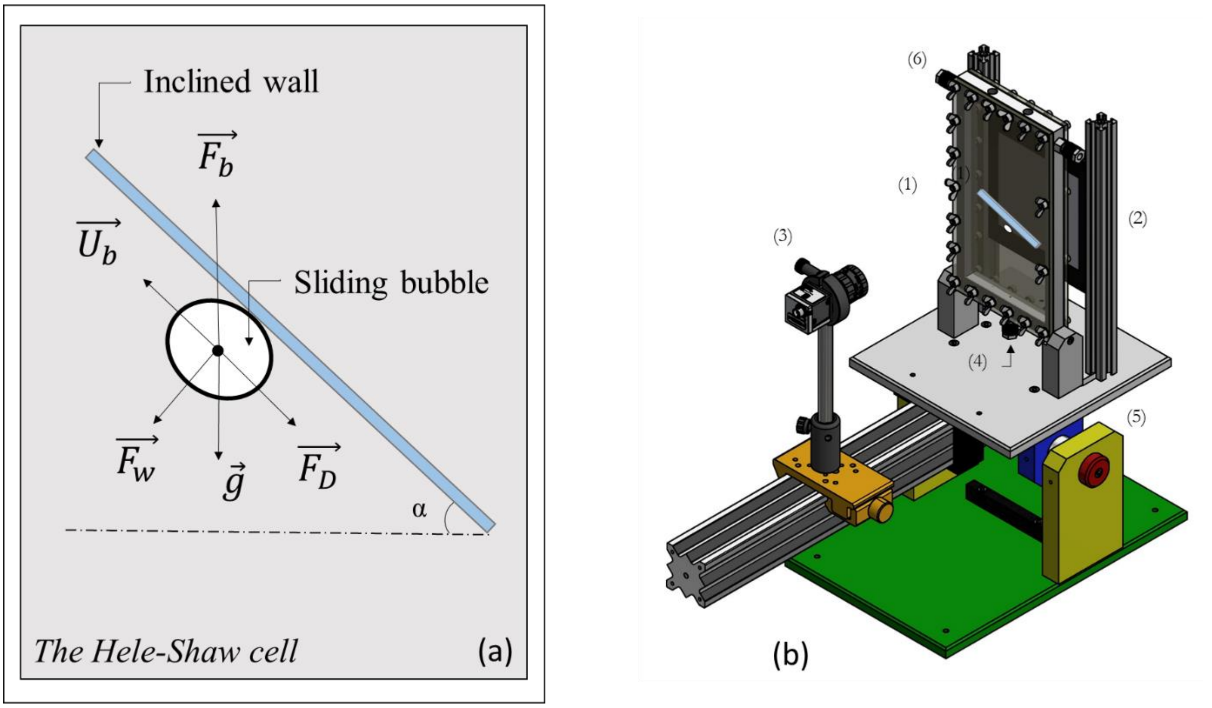

Figure 1 Experimental setup. (a) Diagram of in-plane bubble sliding under an inclined wall of inclination angle α within the Hele-Shaw cell, and (b) 3D representation of the experimental setup (1) Hele-Shaw cell, containing the in-plane confined bubble (white) sliding under the inclined wall (blue) (2) Backlight panel (3) Fast color camera (4) Gas inlet (5) Support for camera and cell (6) Water outlet.

2.2. The colorimetric technique

The colorimetric visualization method (Figure 2a) is a non-intrusive chemical technique based on the use of resazurin, a dye sensitive to the presence of oxygen. This technique had been previously chosen after several tests of different dyes [36]. Its main advantage is that it is non-intrusive and the measurements can be carried out without disturbing the flow by inserting any physical sensor or changing physicochemical properties [12]. In addition to its interesting differences of color (between the colored and colorless states), the choice of resazurin was based on two factors: (i) the fast kinetics of the reaction between dissolved oxygen and dye, and (ii) the intensity of the color generated [36].

The rising bubble was characterized by a pink area in its wake (Figure 2b) caused by the oxidation of dihydroresorufin, which is colorless and not fluorescent, to resorufin, which is pink and highly fluorescent. The later can be obtained from a reduction of resazurin (7-hydroxy-3H-phenoxazine-3-one-10-oxide (molecular mass 229.19 g.mol^{-1})).

The oxidation reaction was made quasi-instantaneous thanks to the use of catalysts, D-glucose anhydrous (Fischer Scientific®, CAS 50–99-7) and sodium hydroxide (VWR®, CAS 1310–73-2), both diluted at 20 g.L^{-1} in deionized water. The back reaction is very slow (few minutes). This dissymmetry between the reaction times makes the method very suitable for high-speed imaging experiments.

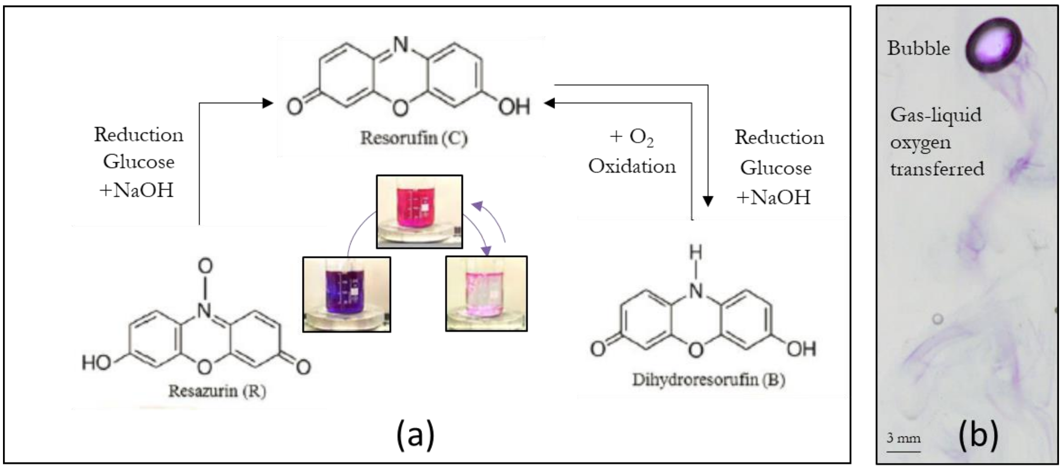

Figure 2: Illustration of colorimetric technique, (a) the technique principle, (b) example of color image of the bubble and the transferred oxygen in its wake.

The physicochemical parameters of the solutions have been thoroughly analyzed [12,36,38]. The density (ρ_L) of the deionized water containing resazurin is 1005.3 ± 0.2 kg.m^{-3}, the dynamic viscosity (μ_L) is 1.1179 ± 0.001 mPa.s and static surface tension (σ_L) is 75.4 ± 0.5 mN.m^{-1}.

When there is a sufficient amount of resazurin to react with all the oxygen transferred, the number of moles of dissolved oxygen can easily be deduced from the number of moles of resazurin [36,37,39]. Note that the purity of the commercial Resazurin was~ 80% and the averaged temperature of experiments was~25 ^{o}C.

2.3. Image acquisition and processing

2.3.1. Image acquisition

The support of the vertical cell also served to support the optical equipment designed to allow the sliding bubble to be clearly visualized using a backlight (Figure 1b). A color camera (Basler acA1920 – 15Ouc, Germany, 8 bits, 144 Hz, 1344 × 1024 pixels^2) was placed horizontally, perpendicular to the cell, and was focused on the center of the cell. The camera was fitted with a 50 mm objective (Micro-Nikkor 50 mm f/2.8, Nikon) to reach a spatial resolution of approximately 0.077 mm/pixel. A backlight panel, providing a soft white light (Phlox, Germany), was placed behind the cell to illuminate the sliding bubble by the shadowgraph technique.

Colored images of oxygen concentrations fields around bubbles sliding in the cell were recorded. The system was calibrated before each experiment so that the dissolved oxygen concentration could be determined from the image recorded. Then, a specific image processing procedure has been proposed.

2.3.2. Image processing

For each resazurin concentration (0, 0.005, 0.05, 0.1, 0.5 and 1 g.L^{-1}), it was possible to associate the observed averaged grey level with a dissolved oxygen concentration for each pixel. An example calibration curve is plotted in figure 3a.

In all the experiments, the resazurin concentration has been chosen of [Dye] = 0.1 g/L (0.08 g/L regarding to the resazurin purity). This concentration is situated in a range of [Dye] ≤ 0.3 g/L where a perfect linearity between grey levels and resazurin concentrations has been found (dashed red line in figure 3a). Therefore, raw color images (Figure 3b-1) can be converted to grey levels, and then into oxygen concentrations using an image processing procedure.

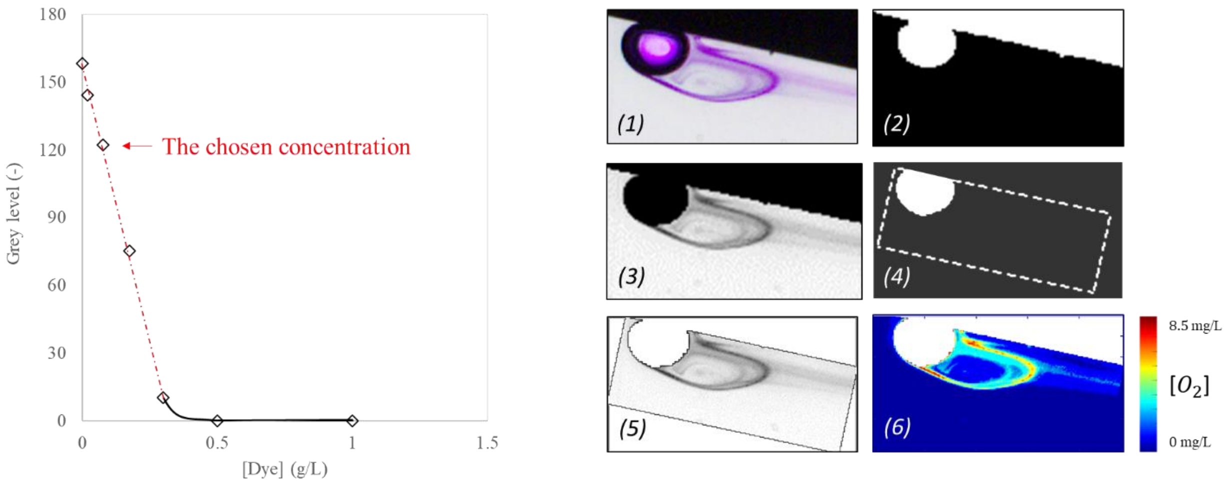

(a)

(b)

Figure 3 Calibration curve (a) and image processing steps (b): (1) Cropped raw image, (2) Detection of bubble and wall (3) Mask the bubble and wall (4) Tracking box based on bubble centroid (5) Liquid containing the transferred oxygen in the box (6) Conversion from grey levels to dissolved oxygen concentration using calibration curve.

The image processing procedure has been performed using the Image Processing Toolbox in Matlab® (R2017b) software. Three main steps were performed:

1. *Cropping images and bubble segmentation:* The colored image were first cropped into an appropriate interested area (shown in Figure 3b-1). The separated red, green and blue components of the images were compared to segment the bubble from liquid background. It has been found that the blue component is more suitable for detecting bubbles edge without affecting the transfer, as the color changing in liquid is pink. Then, the bubble and walls edges were segmented based on threshold in the blue component image (Figure 3b-2). The functions "*imfill*" and "*imsubstract*" has served to fill and mask the bubble and wall. The raw image has been converted to grey value image. Resulted images are then containing only the liquid as shown in figure 3b-3.

2. *Box around detected bubble:* due to the sliding, the bubble and wall were always in contact. When a single bubble was sliding along the wall, oxygen concentration fields appeared in the bubble wake. In order to investigate the oxygen concentration evolution around the bubble during sliding, a box mask was applied to ensure that the area extracted around the bubble was always the same. The box was created using the centroid of the bubble as a reference point regarding to the angle of inclination (Figure 3b-4). All the information and statistics about the position x_b, y_b of the bubble centroid at each position X' on the inclined wall, the equivalent bubble diameter and areas, and the exact angle of inclination, α, of the wall were calculated instantaneously for each configuration via Matlab®.
3. *Conversion of grey level to dissolved oxygen concentration*: Figure 3b-5 illustrates the grey level example of a corrected image containing only the liquid phase inside the box area where grey values represent a certain amount of oxygen transferred by the

bubble. Figure 3b-6 was obtained after the calibration. The total amount of oxygen transferred could easily be determined by summing the estimated concentration pixel by pixel, integrating it over the whole the visualized box.

It is necessary to note that in the case presented in figure 3b, the size of the box was only 400 mm^2. This size, covering just the bubble near wake, was only for illustration purpose, as for figures 7, 8 and 9. However, measurements of dissolved oxygen concentrations (presented in results section 3.2) have taken into account a box that contains the whole path of the bubble, considering both near and far wake. In this case, the size of the box covered the totality of the length of the inclined wall and a width that triple the bubble diameter d_b.

Furthermore, it is important to recall that oxygen concentration measured does not take the thickness of the cell w, related to the bubble wake width, into account when integrating the concentration in the box. This is because the present colorimetric technique is not able to display different planes through the bubble wake width. Therefore, the grey level in each pixel is considered as a sum of oxygen transferred in the dimension w as the calibration is linear in the experimental conditions.

3. Results and discussion

Confined air bubbles with equivalent diameter d_b between 4.54 ± 0.15 mm and 10.94 ± 0.15 mm were sliding under in-plane inclined confined walls with $10° \leq \alpha \leq 60°$ to the horizontal. After releasing the bubble, it impacted the same position X_0', then the bubble started sliding from right to left. Its centroid tracking allowed the determination of positions $X' = X_0' + dX'$ and times $t_B = t_0 + dt$ during sliding. The figure 4 shows an example of bubble under an inclined wall of α=10° at different positions X' (mm) and times t_B (s) during its sliding. Figure 4a represents an overlaid of raw images, recorded from one of the experiments. This figure illustrates also the evolution of the transferred oxygen (pink color) in the bubble wake (Figure 4b).

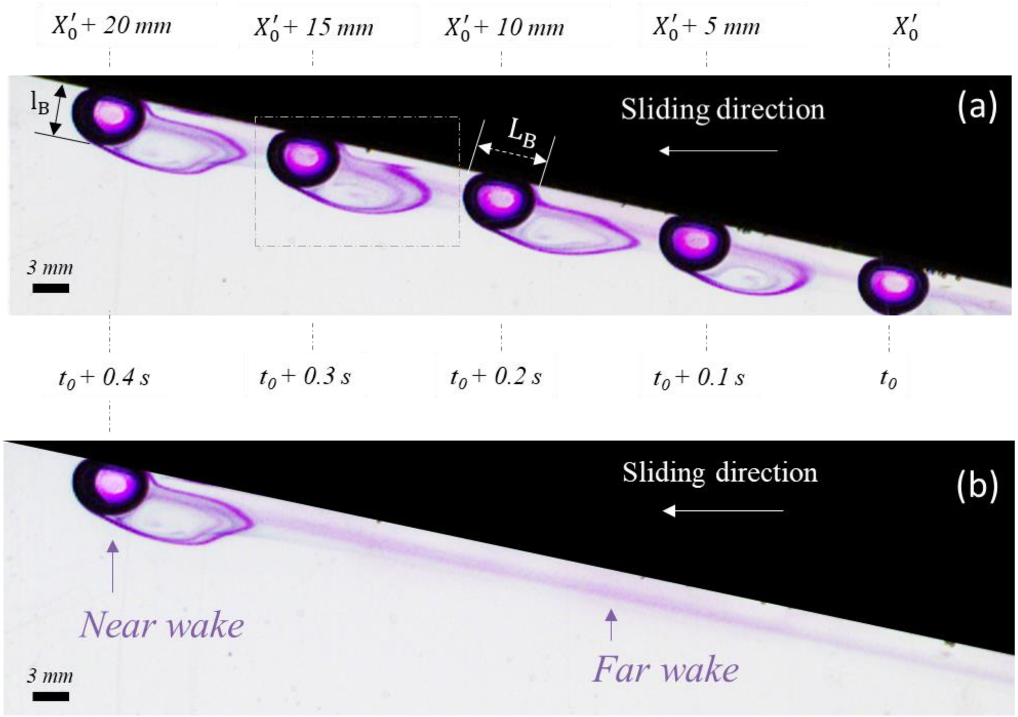

Figure 4 Example of experimental images illustrating both sliding bubble dynamics and its oxygen transfer around for α=10° and bubble equivalent diameter d_b =4.54 ± 0.15 mm (a) overlaid images at different positions X' (mm) and times t_B (s) (b) oxygen transferred around the bubble in both near and far wake.

3.1. Hydrodynamics

The velocity of confined sliding bubbles U_b (m/s) was measured by visualizing and tracking the bubble motion. It represented the time t_B (s) required for the displacement of the confined bubble centroid to cross the distance X' (m).

Table 1 reports the main experimental results of the hydrodynamics around sliding confined bubble. Figure 5 shows the evolution of bubble velocity U_b (m/s) and interfacial area a (m^{-1}) depending on inclination angle α for two different diameters. It has been observed that confined bubble velocities increased when inclination angles α or bubble equivalent diameters d_b

increased. For a confined bubble of d_b = 4.54 ± 0.15 mm, measured velocities at the same distance traveled, *X’*, of 57 mm, were from 48.28 mm/s to 164.16 mm/s, for angles α from 10º to 60º. Furthermore, when d_b increased to reach 10.97 mm, U_b increased from 95.44 mm/s to 235.56 mm/s under the same angle α=30º (Table 1).

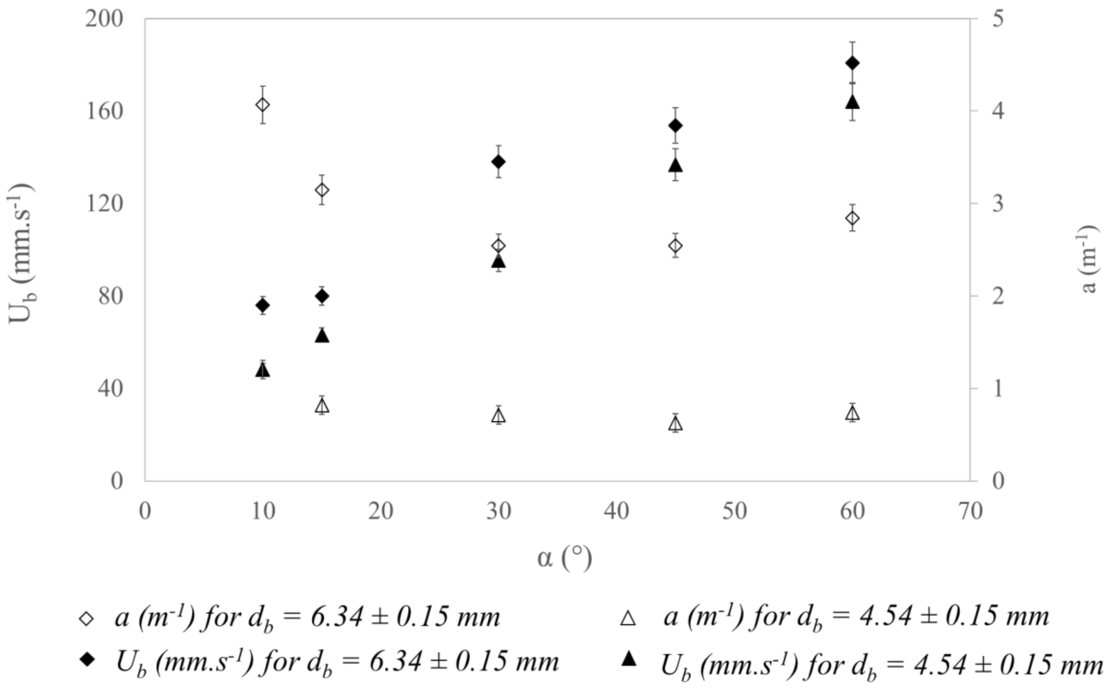

Figure 5 Evolution of U_b (mm.s^{-1}) and interfacial area *a* (m^{-1}) depending on inclination angle α for confined sliding bubbles of equivalent diameters d_b=4.54 ± 0.15 mm and d_b=6.34 ± 0.15 mm measured at the same position *X’*=0.057 m.

On the other hand, during the displacement of a bubble d_b of 4.54 ± 0.15 mm in the dimension *X’*, it has been observed that the bubble centroid had a slight increase of velocities (from 1.2 to 4.4% for α from 10º to 60º). However, under the lowest angle α = 10º, U_b had a constant decrease in *X’* of about 7.7% before it reached its terminal velocity of 48.28 mm/s.

The velocities found were less than their equivalents for free sliding bubbles discussed in the literature. In fact, when α=30º, a free sliding bubble of d_b = 5.76 ± 0.15 mm had a velocity of 183.1 mm/s while it was 215.2 mm/s for free rising bubble [26,27]. However, a confined sliding bubble of approximately the same volume (d_b = 6.34 ± 0.15 mm) had U_b = 137.89 mm/s (Table

1). Confined sliding bubbles are confronted to several forces: the buoyancy due to the upper inclined wall [9,28], and higher inertia due to the confinement [8], which slightly slows down their overall motion.

Table 1. Experimental results of hydrodynamics and gas-liquid mass transfer around a confined sliding bubble

α (°)	d_b (mm)	m_{O_2} ($\times 10^{-6}$ g)	U_b (mm/s)	φ (mg/m^2.s)	a (m^{-1})	k_L (m/s)	k_La (s^{-1})	Re (-)	Ar (-)	Sh (-)
10	4.54 ± 0.15	1.895	48.28	24.66	1.201	1.572×10^{-4}	1.889×10^{-4}	186	792	338
	6.34 ± 0.15	3.542	75.95	35.55	4.068	1.365×10^{-4}	5.552×10^{-4}	451	1498	451
15	4.54 ± 0.15	1.309	63.14	32.76	0.817	2.086×10^{-4}	1.705×10^{-4}	266	903	489
	6.34 ± 0.15	3.155	80.01	32.30	3.148	1.655×10^{-4}	5.211×10^{-4}	476	1503	548
30	4.54 ± 0.15	0.884	95.44	38.33	0.714	2.440×10^{-4}	1.742×10^{-4}	396	884	564
	4.97 ± 0.15	1.318	118.96	36.92	1.374	2.355×10^{-4}	3.237×10^{-4}	531	985	585
	5.40 ± 0.15	1.447	122.51	36.37	1.576	2.321×10^{-4}	3.659×10^{-4}	594	1116	627
	6.34 ± 0.15	2.037	137.89	40.16	2.545	2.278×10^{-4}	5.798×10^{-4}	785	1419	722
	7.74 ± 0.15	2.320	159.07	39.73	3.541	2.151×10^{-4}	7.615×10^{-4}	1107	1917	833
	10.94 ± 0.15	4.356	235.56	42.14	7.727	2.741×10^{-4}	2.117×10^{-3}	2316	3221	1499
45	4.54 ± 0.15	0.687	136.80	48.56	0.628	3.091×10^{-4}	1.941×10^{-4}	524	783	659
	6.34 ± 0.15	2.264	153.82	50.12	2.546	2.823×10^{-4}	7.188×10^{-4}	872	1431	890
60	4.54 ± 0.15	0.809	164.16	58.14	0.740	3.702×10^{-4}	2.741×10^{-4}	668	858	839
	6.34 ± 0.15	2.772	180.75	42.14	2.844	3.635×10^{-4}	10.340×10^{-4}	1073	1499	1201

Before the investigation of the interfacial area shown in figure 5, it is worthwhile to characterize the effect of the inclined wall on the bubble shape elongation. For this purpose, we introduce the shape eccentricity, e, which describe the circular aspect of the bubbles given by $e = \sqrt{1 - \frac{L_B}{l_B}}$, where L_B and l_B are the bubble major and minor axes, respectively. An eccentricity of 0 is a perfect circle, while an eccentricity of 1 is a flat line. The evolution of eccentricity of the bubble as function of the inclination angle is depicted in figure 6.

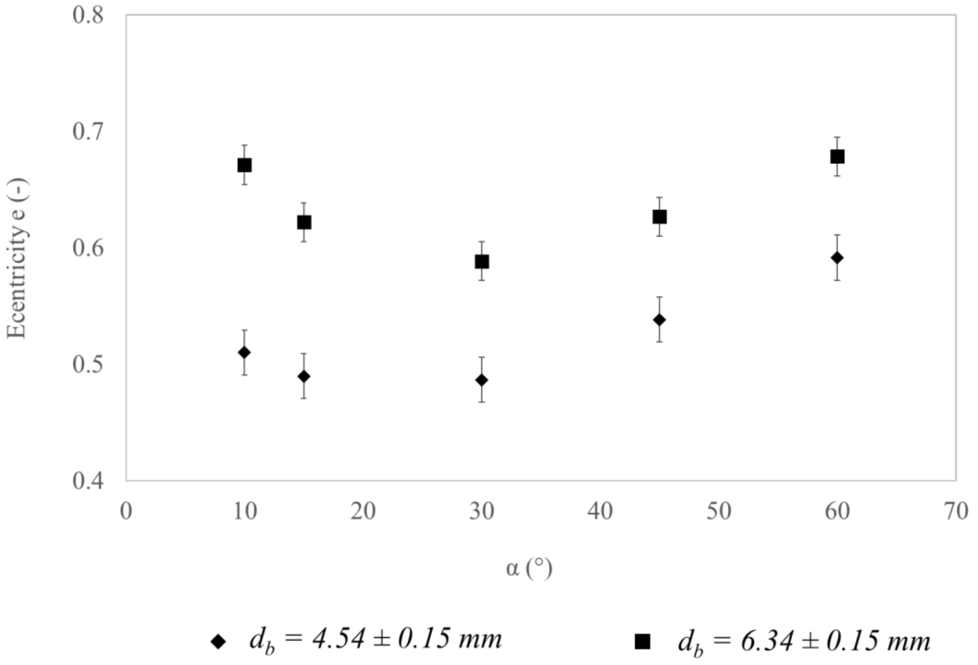

Figure 6 Evolution of eccentricity, *e*, depending on inclination angle α for confined sliding bubbles of equivalent diameters d_b=4.54 ± 0.15 mm and d_b=6.34 ± 0.15 mm.

Experiments revealed that the decrease of wall inclination angle increase bubble eccentricity, within a limit, as shown in figure 6. When α= 60º, a well-defined ellipsoidal bubble of e=0.59 was found (d_b= 4.54 ± 0.15 mm) but, when α started to approach 30 º, e decreased and reached a minimum of 0.48, showing the most circular shape observed for any tested angle. For the angles closest to 10º, the bubble shape elongated under the inclined wall around its major axis, increasing the eccentricity to 0.51. However, when d_b increased, eccentricities were more pronounced at both low and high angles following the same trend (Figure 6).

The interfacial area, *a* (m^{-1}), is an important parameter that characterize the mass transfer. It is expressed in relation 1 as:

$$a = \frac{S_G}{V_T} = \frac{S_b}{V_b + V_L + V_S} \qquad (1)$$

Where S_G (m^2) is the total surface area of the gas phase in the Hele-Shaw cell, defined as the surface area of the single bubble released for each configuration, S_b (m^2). V_T (m^3) is the whole volume of gas/liquid/solid phases in the cell.

Since all the bubbles in this study have $d_b > 4$ mm, with factor of confinement $f << 1$, the surface of the confined bubble can be described as a cylinder, that takes into account the equivalent diameter d_b, in its ellipsoid base, and thickness of the cell as its height.

The evolutions of a (m^{-1}) in function of the angle α are plotted in the figure 5. Maximum values of 4.067 m^{-1} and 1.204 m^{-1} were found at low angles of 10°, respectively for $d_b = 6.34 \pm 0.15$ mm and $d_b = 4.54 \pm 0.15$ mm. When the angle increased, the interfacial area decreased, to reach a minimums of 2.545 m^{-1} and 0.628 m^{-1} respectively at 45 ° and 30 °, then, a started a slight increase and reached respectively 2.844 m^{-1} and 0.741 m^{-1}. Those results of interfacial area can be explained by the effect of the eccentricity on bubble elongation previously reported.

Therefore, it has been found that velocities of sliding bubble were increased with increasing wall inclination angles and increasing bubble sizes. For low angles $\alpha<30°$, the bubble shape was elongated and shows high interfacial areas while their velocities were decelerated. For high angles $\alpha>30°$, the little effect of the wall inclination led the ellipsoidal bubble shapes to be almost unchanged showing higher velocities of their centroid. Between those two ranges, bubbles were more circular than ellipsoidal and their interfacial areas measured were minimum.

3.2. Gas-liquid mass transfer

The spatial and temporal distribution of oxygen concentration fields during sliding was visualized and illustrated in figures 7, 8 and 9. The obtained images shows blue regions corresponding to where there was no oxygen, whereas white regions corresponded to the masked bubble and upper wall. Other color areas corresponded to oxygen concentrations in the liquid according to the colormaps depicted on each figures.

The evolution of the oxygen concentration fields for a bubble of d_b = 4.54 ± 0.15 mm has been shown for an inclination angle of α= 10º in figure 7. This figure provides the instantaneous equivalent O_2 concentration fields underneath the sliding bubble at nine instants in time, 0.08 s apart, at different positions X'. From the moment when the bubble starts sliding, oxygen starts transferring through a distinct region at its interface (delimited by a dashed red circle in figure 7 at t_{B1}=0.30 s). As time went on, a steady generation of a vortex loop appears and grows in the counter clockwise direction of motion. Meanwhile, oxygen starts accumulating and convection in the bubble wake region is occurring. The size of the wake is approximately 1.5 times the bubble size. This vortex loop enclosing the near wake reaches its maximum size at 0.86 ms and maintains it as a steady state behavior.

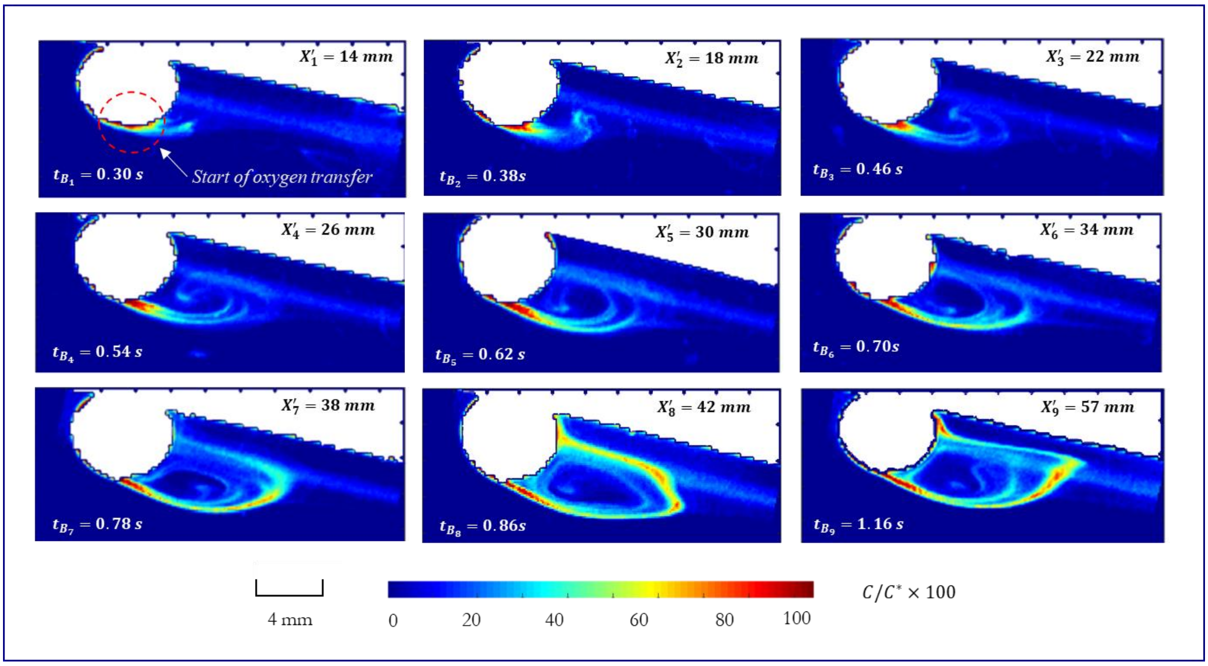

Figure 7 Evolution of oxygen concentrations fields at the near wake of a confined bubble d_b=4.54± *0.15 mm* under $\alpha = 10\ ^o$ during its sliding for 0.30 s < t_B < 0.94 s, and 14 mm <*X'*< 57 mm at *Ar*=792.

Figure 8 illustrates the effect of wall inclination α on O_2 concentration fields, under different sliding distances *X'* chosen at 0 mm, 30 mm and 40 mm for illustration purpose, for different inclination angles from 10º to 60º at the same Archimedes number of 800. In those conditions, oxygen has accumulated in the same regions underneath the bubble shown above in figure 7. It appears that the oxygen starts transferring through the same distinct region at the bubble interface shown previously, and accumulates in the bubble wake region. However, it has been observed that the vortex loop has extended its shape with increasing angles, from 1.5 times the bubble size at 10° to 3 times the bubble size at 30°. However, it become difficult to observe the steady generation of the vortex when the angles of inclination became higher than 45°. It seems that this vortex detaches prematurely as bubbles were faster under higher angles, and no stabilized vortex loop has been observed.

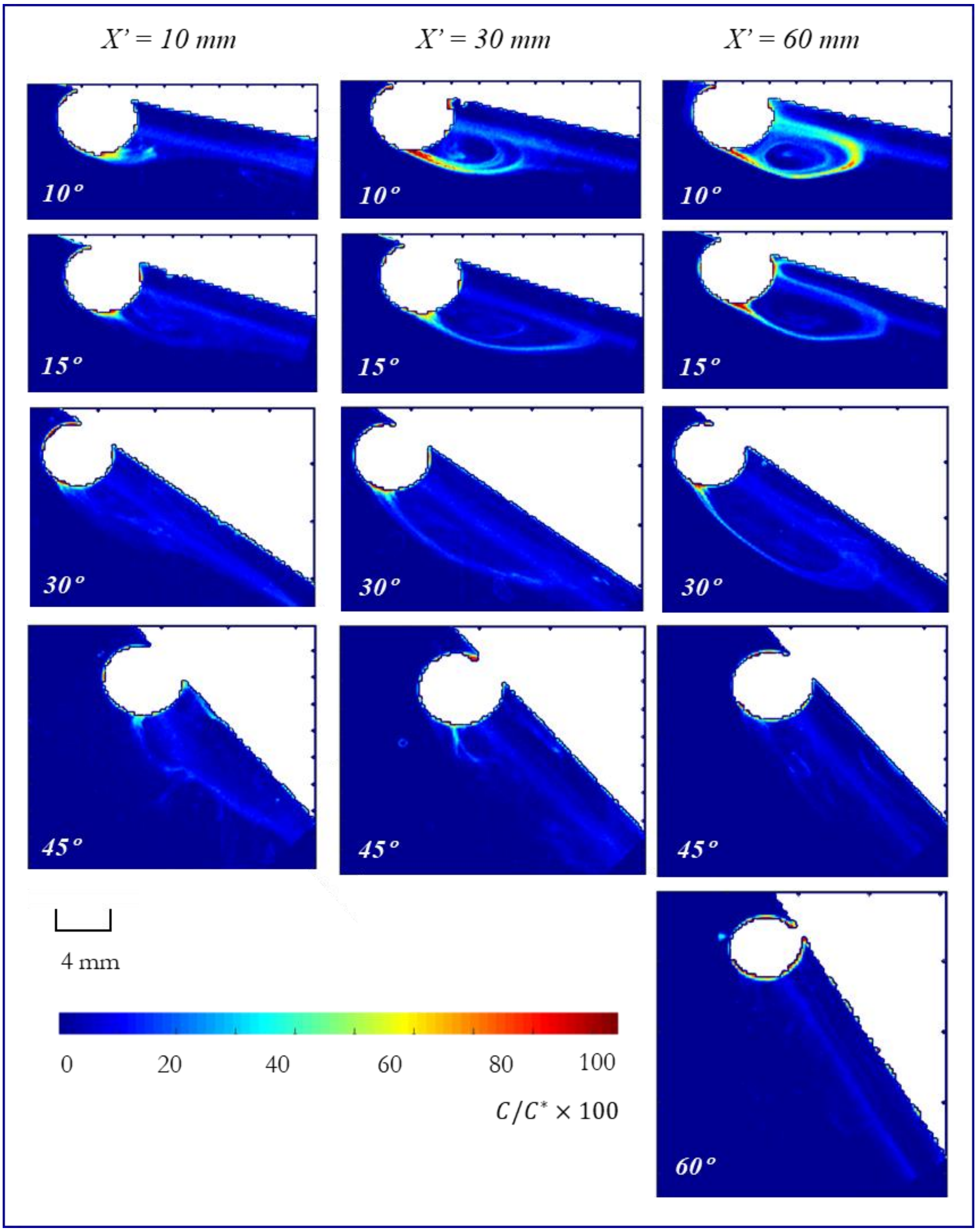

Figure 8 Evolution of oxygen concentration fields in the near wake of a confined bubble d_b=4.54± 0.15 mm for 10º < α < 60º at different positions *X'* of 10, 30 and 60 mm at *Ar=800*.

Finally, figure 9 illustrates the effect of increasing bubble size on oxygen concentrations fields for Archimedes numbers from 884 to 3221 under the same angle of inclination 30º. This figure shows that the near wake, where oxygen transferred from the same distinct region (Figure 7), enlarge with increasing *Ar*, but seems to keep the same ratio of about 3 times the bubble size. Moreover, the steady vortex loop observed in low Archimedes numbers (884) transit gradually to a less structured wake showing more instabilities underneath increasing bubble sizes (from 6 to 10.94 mm) (Figure 9d,e). In those conditions, the near wake was more and more turbulent. At the end, it becomes more difficult to ascertain individual vortex loops at Ar=3221, and the unstable behavior on the wake indicates that more turbulent mixing of dissolved oxygen took place underneath large sliding bubble (Figure 9f).

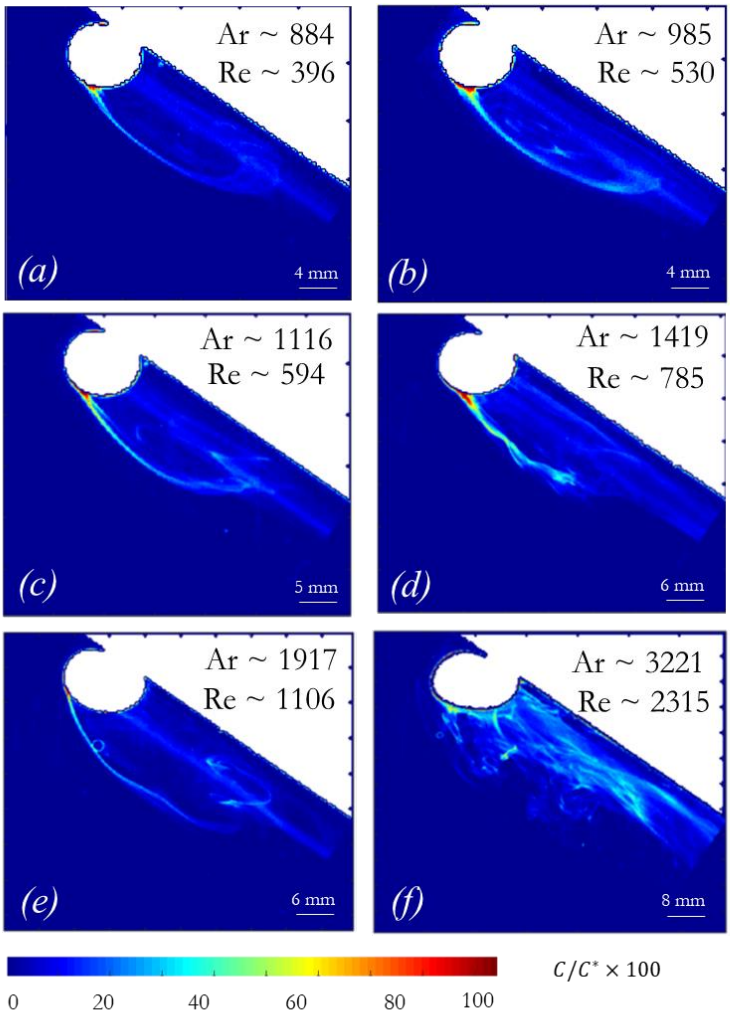

Figure 9 Evolution of Oxygen concentration fields in the wake of confined bubbles of $4.54 < d_b < 10.94$ mm, $883 < Ar < 3221$, $396 < Re < 2315$ under $\alpha = 30°$ at the same *X'* = 57 mm.

From the analysis of figures 7, 8 and 9, it was found that oxygen concentration fields underneath the sliding bubble had different shapes that could be separated according to two ranges of inclination angles, α.

1. For $\alpha \leq 45^{o}$, a single vortex pattern enclosing the transferred oxygen was found, which grew during sliding depending on time (Figure 7), on the position *X'* and the inclination α (Figure 8), and on the size of the bubble (Figure 9). In this range, two distinct parts were identified in the bubble wake:
    a) *The bubble near wake:* Once the bubble started sliding, oxygen began to accumulate underneath the bubble. Transferred oxygen has been located in a steady recirculation zone enclosed by a counter-clockwise single vortex leg. The transferred O_2 was collected and convected in a region attached to the bubble. As the time increased, the attached single vortex enlarged and reached its maximum size that was approximately 1.5 times the bubble size, and the regime started to enter a steady state (Figure 7). At this time (0.86 ms), the local O_2 concentration underneath the bubble seems to be maximum and remained stable, at least in the range of bubbles tested (4.54 mm to 10.94 mm). However, when α increased, the previously found vortex loop extends its shape with increasing angles, from 1.5 times the bubble size at 10° to reach 3 times its size at 30° (Figure 8). However, this ratio seems to be the same under the same inclination angle when bubble sizes were increasing. In those conditions, a gradual transit from a steady vortex loop in low Archimedes number of 884 to a less structured wake showing more instabilities at high Archimedes number of 3221 has occurred.
    b) *The bubble far wake:* a straight strip of oxygen, resembling a long filament, remained behind the bubble, under the inclined wall, throughout the sliding distance (Figure 4b). This tail looked like a filament observed underneath the bubble rising

in the rectilinear regime [23]. This single tail, located in the far wake showed lower O_2 concentration than the near wake. For example, for $\alpha = 10°$, only 33.74% of [O_2] was deposited in the far wake that represent more than 90.21% of the box area where the bubble has traveled.

2. For $\alpha \geq 45°$, it was difficult to observe the previous two distinct regions (Figure 8) due to increased bubble velocities. This did not allow the convection of vortex loop to the bubble. Therefore, the vortex detaches prematurely in the bubble wake and vortex loops are no longer observed.

It is noteworthy, that the vortex leg did not detach from the bubble beneath for angles $\alpha \leq 30°$, because of the in-plane confinement conditions that force a rectilinear behavior of bubble. It is well known that, vortex detachment needs a ‘zig-zagging’ bubble behavior, where vortex shedding is occurring at points where bubbles changes their trajectory directions, called, “the inversion point” [26,28,33]. This was not observed in this study, at least for the range of inclination tested from 10° to 60°. Moreover, it has been found in literature that, unlike what we have observed for confined sliding bubbles, free sliding bubbles could allow hairpin vortex separation at different “inversion points” on the bubble trajectory leading to several vortices under the upper wall in the far wake. However, in this 2D study, the bubble did not manifest a ‘zig-zagging’ behavior, which forces the attachment of the single vortex to the sliding bubble, allowing only a single tail to be observed far behind the confined sliding bubble parallel to the inclined wall.

The aforementioned oxygen transfer visualization has allowed the measurement of the mass of oxygen $m_{o_2} = \iiint C(x,y) \cdot dx \cdot dy \cdot dz$, transferred instantaneously in the wake of the bubble.

Figure 10 shows the results of the mass of oxygen transferred as function of angle of inclination. It has been shown that m_{o_2} decreased gradually with increasing angles within a certain limit. For α = 10°, m_{o_2} was 1.90×10^{-6} g and decreased to reach a minimum 0.68×10^{-6} g at α = 45° for d_b=4.54 ± 0.15 mm (Table 1). However, if the bubble size was larger, e.g., when d_b = 6.34 ± 0.15 mm, m_{o_2} showed the same trend but was almost two times bigger than for d_b=4.54 ± 0.15 mm, and the minimum of 2.03×10^{-6} g has been reported at α = 30° (Figure 10).

Dividing this mass m_{o_2} by the time t_B taken by the sliding bubble, of a surface S_b (m^2) to reach *X'* position under the inclined wall, leads to the mass flux density:

$$\varphi(X') = U_b \cdot \frac{\partial \bar{C}}{\partial X'} = \frac{U_b . E}{X' \cdot S_b} \iiint C(x, y) \cdot dx \cdot dy \cdot dz \qquad (2)$$

Where U_b (m/s) is the bubble velocity, $\overline{C}$ (g/L) is the averaged dissolved oxygen concentration accumulated in the box under the wall when the bubble is at the axial position *X'* (m). *E* is an enhancement factor (*E* = 1 in our condition) [39].

Figure 11 illustrates the evolution of the mass flux depending on the *X'* position. It has been found that $\varphi(X')$ slightly increased in *X'* dimension. For low angle 10°, an increase in mass flux has been occurred from 17.86 to 23.21 $mg.m^{-2}.s^{-1}$. This increase can be explained by the accumulation of the transferred oxygen during the sliding. It coincides with the development of the vortex loop shown in figures 7 and 8. In addition, when the angle of inclination increased, an increase of mass flux has been noted for the same bubble size. Results in Table 1 shows that, for the same position *X'*=57 mm. For a bubble of d_b=4.54 ± 0.15 mm, the flux increased from 24.66 $mg.m^{-2}.s^{-1}$ to 58.14 $mg.m^{-2}.s^{-1}$ for inclination angles from 10° to 60°, while it increased from 35.55 $mg.m^{-2}.s^{-1}$ to 42.14 $mg.m^{-2}.s^{-1}$ for d_b=6.34 ± 0.15 mm under the same angles.

This result is very important and proves the importance of increasing velocities on improving mixing and renewal of bubble interface. In fact, although what has been shown in figure 7 and

8, where oxygen looks more concentrated at low angle (α<30°), mainly in the near wake region that represented only 1.5 times the bubble size. However, mass flux results has proven that the decrease of velocity at low angles cause less mixing in the liquid, showing less mass flux (Figure 11). In addition, this might explain also the steady generation of the well-defined vortex occurred at low angles. However, at high angles (α>30°), the increase of mass flux can be explained by the increase bubble velocity producing gradually more mixing in the liquid.

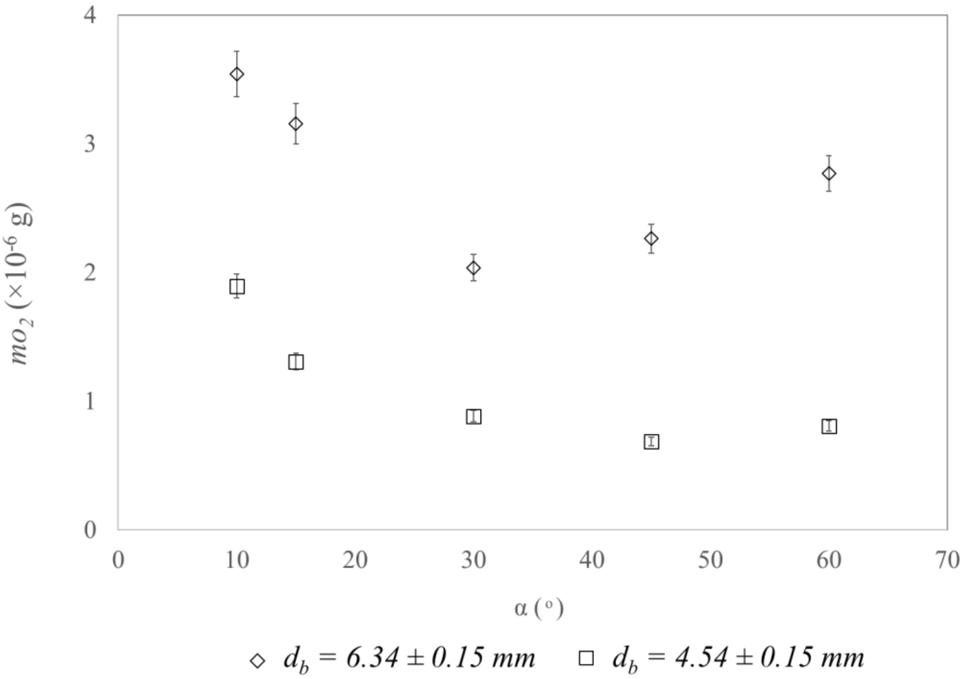

Figure 10 Transferred mass m_{O2} (g) depending on inclination angle α for confined bubbles of equivalent diameters d_b=4.54 ± 0.15 mm and d_b=6.34 ± 0.15 mm at the same position X'=0.057 m.

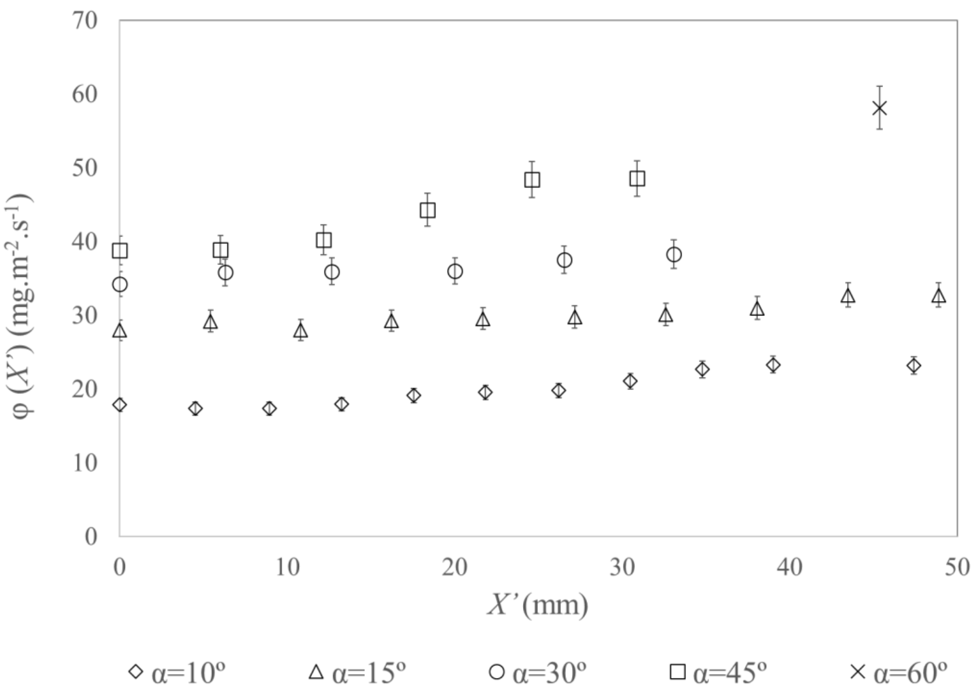

Figure 11 Evolution of mass flux density $\varphi(\mathrm{X}')$ as function of *X'* during sliding of a bubble having d_b=4.54±0.15 mm at *Ar* = 800 at different angles of inclination.

Furthermore, Roudet et al., [6] has explained that mechanisms of mass transfer are depending on the contact between the bubble and the solid walls. This can contribute to the result of mass flux. In fact, the surface of bubbles in Hele-Shaw cell can be in simultaneous contact with (1) the liquid film located between bubble and the plates of the Hele-shaw cell [6]; (2) the liquid filling the thin gap cell. They found a predominance of the contribution of the liquid film against mass flux, contributing to 87% of the total mass flux compared to the peripheral region, for a free confined bubble at *Ar*=1200. However, a third area has been identified in the present study. The sliding confined bubble could have, indeed, a contact with (3) the upper wall. This area is located between the upper side of the bubble and the inclined wall. Even this contact area is representing only from 0.57% to 4.35% of the bubble surface depending on the angle of inclination, and the bubble size. However, it is hard to conclude about its contribution to the mass transfer in this study, since it is still unknown if the liquid film involved between the bubble and the inclined wall can be considered as lubrication film.

Therefore, oxygen could be considered as simultaneously transferring through those three surfaces. The contact between the bubble and the three main components of the Hele-Shaw cell leads to combined previous result of the total mass flux $\varphi\ (X')$, and then contribute to the calculation of the liquid-side mass transfer coefficient k_L (m/s) using relation 3.

$$\varphi\ (X') = k_L \cdot a \cdot C^* \qquad (3)$$

Where a (m^{-1}) is the interfacial area between gas and liquid, and C^* is the dissolved oxygen concentration at saturation (C^*~8.15 mg/L). The concentration of dissolved oxygen in the liquid at the scale of the unit cell is zero, due to its consumption by the chemical reaction [39].

Combining equations 2 and 3 leads to relationship 4, which, integrated over the entire box, leads to the k_L coefficient in equation 5.

$$\frac{\partial \bar{C}}{\partial X'} = \frac{k_L \cdot a \cdot C^*}{U_b} \qquad (4)$$

$$k_L = \frac{\overline{C} \cdot U_b}{a \cdot X' \cdot C^*} \qquad (5)$$

The liquid-side mass transfer coefficient k_L is plotted versus the inclination angle α in figure 12. It has been found that the coefficient k_L increased with increasing inclination angles and therefore velocities (Table 1). For bubble size d_b=4.54 ± 0.15 mm, k_L increased from 1.57×10^{-4} m/s to 3.70×10^{-4} m/s for inclination angles from 10° to 60° where bubble velocities were respectively increasing from 48.28 mm/s to 164.16 mm/s. However, when the bubble size increased to d_b=6.34 ± 0.15 mm, the liquid-side mass transfer coefficient has decreased by about 13.19% compared to that from bubble size d_b=4.54 ± 0.15 mm. This result is in accordance with studies of previous mass flux results and corroborate mass transfer trends in literature. In fact, the increase of bubble velocities, affected by increasing wall inclinations, can increase liquid mixing in the liquid [34]. In addition, it can provides more renewal at the bubble interface [35].

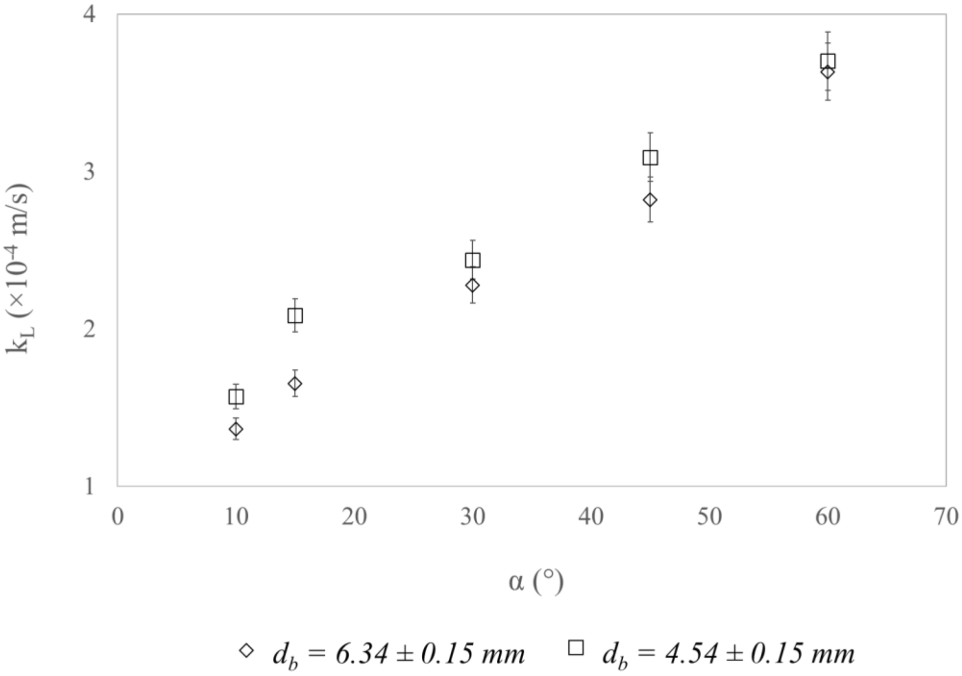

Figure 12 Evolution of liquid-side mass transfer coefficient (m/s) depending on inclination angle α for confined sliding bubbles of equivalent diameters d_b=4.54 ± 0.15 mm and d_b=6.34 ± 0.15 mm.

In order to provide an analysis of all the results found and the effect of the in-plane inclination angles and bubble sizes on the mass transfer outcomes. It is relevant to introduce the Sherwood number that controls the mass transfer $Sh = \frac{k_L d_b}{D}$, where k_L (m/s) is the liquid-side mass transfer coefficient, d_b (m) is the equivalent diameter of the bubble, and D (m^2/s) is the diffusion coefficient [11,25,40]. In addition, the dimensionless Peclet number $Pe = \frac{U_b d_b}{D}$ involves the bubble velocity U_b and its equivalent diameter d_b (m) [6].

A scaling law that highlights the evolution of Sherwood number with Archimedes numbers and Peclet numbers while taking the angle of inclination α into consideration (Figure 13) can be proposed. This law, *Sh(Ar.sinα),* has been used for 15 points from the experimental results in a range of inclination angles 10° ≤ α ≤ 60° and Archimedes numbers 700 ≤ Ar ≤ 3221.

Under those experimental conditions, a satisfactory fitting of the experiments has been obtained for the equation 6. It has been found that the experimental results have verified this correlation for a standard deviation of 9%.

$$Sh = \frac{2}{\sqrt{\pi}} \cdot (Pe)^{\frac{1}{2}} \cdot \sin(\alpha) + \frac{1}{3} \cdot Ar \cdot \cos(\alpha) \qquad \textit{(6)}$$

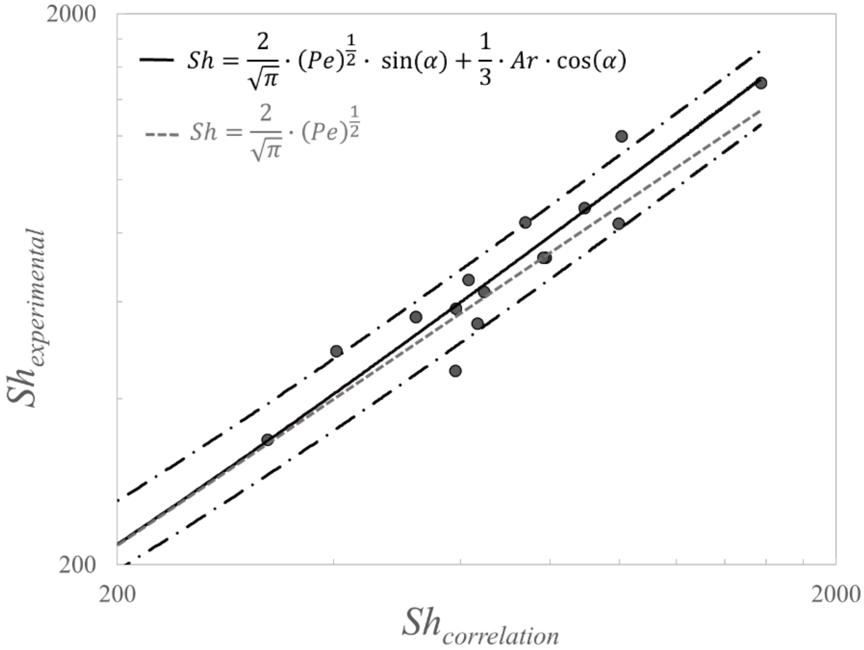

Figure 13 Scaling law for gas-liquid mass transfer around sliding bubble depending on inclination angle α.

Using this scaling law, the mass transfer can be compared to that occurring at the interface of rising bubbles with the same volume, but depending on inclination angles α of the upper wall.

Previously, Roudet et al., [6] has mentioned the scaling law $Sh = \frac{2}{\sqrt{\pi}} \cdot (Pe)^{\frac{1}{2}}$. However, for sliding bubbles, where bubble velocities can be lower compared to rising bubbles, it has been possible to introduce a modified Archimedes and Peclet number depending on α. Therefore, the law proposed in this study (Equation 6) could link two terms of effects depending on the angle of inclination:

- The first term $\frac{2}{\sqrt{\pi}} \cdot (Pe)^{\frac{1}{2}} \cdot \sin(\alpha)$ of the correlation, presents the scaling law applied by Roudet et al., [6] for confined bubbles but modified depending on the inclination angle. This term can be predominant at high inclination angles. It can shows that high bubble velocities and larger sizes can predominantly affect the mass transfer when the inclined wall become near to the vertical.
- The second term: $\frac{1}{3} \cdot Ar \cdot \cos(\alpha)$, preponderant at low inclination angles, where the effect of the inclination angle α together with bubble size can be preponderant against mass transfer.

It is also possible to extend this law for confined rising bubbles by assuming the case where bubbles are rising freely in confined medium (near a vertical wall). In this configuration, the second term is mostly predominant while the first one will be neglected, which is in total accordance with the scaling law shown by Roudet et al., [6]. At the end, from this law, it has been found that increasing angles of inclination increased the mass transfer in the system by increasing bubble velocities.

Global discussions

For the lowest angles tested $\alpha = 10°$ when $Ar \leq 900$, the instantaneous spatial and temporal distribution of oxygen concentration fields revealed two distinct regions, where oxygen transferred mostly (~75%) in the small region in the near wake that represented a vortex loop

(Figure 7), while the rest of oxygen concentrations was released in the far wake. Even if in figure 7 and 8, oxygen looks more concentrated in the near wake, however, it remains enclosed in a small area that represented only 1.5 times the bubble size. Less mixing has been occurred. The sliding bubbles were then characterized by the lowest mass fluxes (Table 1). The decrease of velocity at low angles has decreased the liquid-side mass transfer coefficient k_L. Sherwood numbers has been then the lowest ($Sh < 480$) in this range. As the angles of inclinations started to increase from 15° to 45°, and so were the bubble sizes ($900 \leq Ar \leq 1500$), oxygen concentrations fields has shown that the vortex leg, which was occurring at low angles, extended from the bubble beneath as the angle of inclination increase. This vortex has been separated prematurely if $\alpha > 30°$ before it forms a loop (Figure 8). On the other hand, the transition regime from the steady vortex leg to an unstable one has occurred gradually depending on bubble size. In addition, the size of the near wake seems to depend on the bubble size at the same $\alpha = 30°$ (Figure 9). Based on the calculations of oxygen concentrations, mass fluxes were increasing. The liquid-side mass transfer coefficient k_L continued to increase with increasing inclination angles and bubbles sizes and so *Sh* has been increasing between 480 and 830.

Finally, for high angles of inclination $\alpha \geq 45°$ when $1419 < Ar < 3221$ (Figure 13), bubbles velocities were the highest. The liquid-side mass transfer coefficient marked the highest values noted of all the experiments (Table 1). Turbulences underneath bubbles were more pronounced, since the oxygen concentration fields shows no vortex formation underneath the bubble and more mixing in the bubble wake (Figure 9f) while the Sherwood number *Sh* in this range has reached *1500*.

4. Conclusion

The aim of this original experimental research was to investigate the instantaneous gas-liquid mass transfer induced from a single confined bubble sliding under an inclined wall. Experiments were performed in a Hele-Shaw cell using a colorimetric technique based on oxygen sensitive dye (resazurin) to visualize oxygen transfer. Thanks to the calibration performed for each experiment, and through image processing, the instantaneous spatial and temporal evolution of transferred oxygen concentration fields has been quantified, for the first time, around sliding bubbles. A specific image processing made possible the calculation of the mass flux and liquid-side mass transfer coefficients. Furthermore, the effect of the inclination angle α and bubble size on the dynamics of the bubbles and gas-liquid mass transfer has been investigated. Finally, a scaling law highlighting the evolution of the Sherwood number as a function of the Archimedes numbers and the angle of inclination, α, has been proposed.

Experiments reveals that, for the lowest angles tested $\alpha = 10°$ when $Ar \leq 900$, and due to the wall inclination, velocities of confined bubbles decelerated, and the eccentricity of their shapes increased. Evolution of the dissolved oxygen concentration fields revealed two distinct regions in the wake of the bubble while sliding, in which oxygen transferred mostly in the near wake enclosed by a vortex loop rather than the long straight strip released in the far wake. However, the decrease of velocity at those low angles has decreased the mass fluxes and the liquid-side mass transfer coefficient k_L. Sherwood numbers has been then the lowest in this range.

As the inclination angle started increasing, from 15° to 45° when $900 \leq Ar \leq 1500$, bubble velocities increased, and the eccentricity of their shape were more circular than ellipsoidal, with a decrease in their interfacial areas. Oxygen concentrations fields has shown that the vortex leg has extended from the bubble near wake as the angle of inclination increase. A transition from the steady vortex leg to a turbulent structure of oxygen concentrations has occurred gradually depending on increasing bubble size. Measurement of oxygen concentrations has shown an increase in mass flux when angle of inclinations increases, creating more mixing in the liquid phase in both near and far wake, therefore, the liquid-side mass transfer coefficient k_L continued its increase to reach the highest values of $Sh=1500$ when $\alpha \geq 45°$ and $1419 < Ar < 3221$.

Therefore, from what it precedes, we conclude that increasing upper wall angles and bubbles sizes, is accelerating bubble velocities which lead to an increase in the liquid-side mass transfer coefficient k_L.

This experimental investigation has contributed on understanding the evolution of oxygen concentration fields around single confined sliding bubbles for the first time. It shows how oxygen concentrations fields behave underneath sliding bubbles after gas-liquid mass transfer depending on angle of inclinations. This original study provides more explanations about the contribution of inclined configurations on mass transfer in multi-phase reactors and bring new insights into enhancing gas-liquid mass transfer performances in gas/liquid/solid reactors.

Acknowledgment

The authors specially thank Mr. José Moreau at LISBP for the design of the experimental setup and for providing the sketch. The financial support from the National Natural Science Foundation of China (grant nos 11542016 and 11702210), the 111 project (B18040), and the China Postdoctoral Science Foundation (63th edition, number 3115200043) are gratefully acknowledged for their support of this project.

Nomenclature

a	*Interfacial area* (m^{-1})
C	*Dissolved oxygen concentration at time t* ($g\cdot l^{-1}$)
C^*	*Dissolved oxygen saturation concentration* ($g\cdot l^{-1}$) (C^*)
Ci	*Concentration of compounds* ($g\cdot l^{-1}$)
D	*Diffusion of oxygen*
d_b	*Bubble equivalent diameter (mm)*
e	*Eccentricity of the sliding bubble (-)*
f	*Bubble confinement factor*
$\overrightarrow{F_b}$	*Buoyancy force*
$\overrightarrow{F_D}$	*Drag force*
$\overrightarrow{F_w}$	*Force applied from the inclined wall*
GL	*Grey level*
k_L	*Liquid-side mass transfer coefficient* ($m\cdot s^{-1}$)
$k_{L;}a$	*Volumetric mass transfer coefficient* (s^{-1})
L_b	*Bubble major axis (m)*
l_b	*Bubble minor axis (m)*
m_{O2}	*Total mass transported (g)*
PLIF	*Planar Laser Induced Fluorescence*
PMMA	*PolyMethylMethAcrylate*
PVC	*Polyvinyl chloride*
t_0	*Time at X’=0, start of bubble sliding (s)*
t_B	*Time at X' during sliding (s)*
U_b	*Bubble velocity* ($m\cdot s^{-1}$)

V_G	*Gas volume* (m^3)
V_T	*Total volume* (m^3)
V_B	*Bubble volume* (m^3)
V_L	*Liquid volume* (m^3)
Vs	*Solid volume* (m^3)
w	*Hele-Shaw cell thickness (m)*
X'	*Bubble sliding distance under the inclined wall (m)*

Ar	*Archimedes number,* $Ar = \frac{\rho_L \, d_b \sqrt{g d_b}}{\mu_L}$
Pe	*Peclet number,* $Pe = \frac{U_b d_b}{D}$
Re	*Reynolds number,* $Re = \frac{U_b d_b}{\mu_L}$
Sh	*Sherwood number,* $Sh = \frac{k_L d_b}{D}$

α	*Angle inclination of inclined surface* (^{o})
μ_L	*Dynamic viscosity of the liquid (mPa.s)*
ρ_L	*Density of the liquid* ($kg\cdot m^{-3}$)
σ_L	*Static surface tension* ($mN\cdot m^{-1}$)
φ	*Mass flux density* ($g\cdot m^{-2}\cdot s^{-1}$)

Table legends

Table 1.	Experimental results of hydrodynamics and gas-liquid mass transfer around a confined sliding bubble

Figure legends

Figure 1	Experimental setup. (a) Diagram of in-plane bubble sliding under an inclined wall of inclination angle α within the Hele-Shaw cell, and (b) 3D representation of the experimental setup (1) Hele-Shaw cell, containing the in-plane confined bubble (white) sliding under the inclined wall (blue) (2) Backlight panel (3) Fast color camera (4) Gas inlet (5) Support for camera and cell (6) Water outlet.
Figure 2:	Illustration of colorimetric technique, (a) the technique principle, (b) example of color image of the bubble and the transferred oxygen in its wake.
Figure 3	Calibration curve (a) and image processing steps (b): (1) Cropped raw image, (2) Detection of bubble and wall (3) Mask the bubble and wall (4) Tracking box based on bubble centroid (5) Liquid containing the transferred oxygen in the box (6) Conversion from grey levels to dissolved oxygen concentration using calibration curve.
Figure 4	Example of experimental images illustrating both sliding bubble dynamics and its oxygen transfer around for α=10° and bubble equivalent diameter d_b =4.54 ± 0.15 mm (a) overlaid images at different positions X' (mm) and times t_B (s) (b) oxygen transferred around the bubble in both near and far wake.
Figure 5	Evolution of U_b (mm.s^{-1}) and interfacial area a (m^{-1}) depending on inclination angle α for confined sliding bubbles of equivalent diameters d_b=4.54 ± 0.15 mm and d_b=6.34 ± 0.15 mm measured at the same position X'=0.057 m.
Figure 6	Evolution of eccentricity, e, depending on inclination angle α for confined sliding bubbles of equivalent diameters d_b=4.54 ± 0.15 mm and d_b=6.34 ± 0.15 mm measured at the same position X'=0.057 m.

Figure 7	Evolution of oxygen concentrations fields at the near wake of a confined bubble d_b=4.54$\pm$ $0.15\ mm$ under $\alpha= 10\ ^o$ during its sliding for 0.30 s < t_B < 0.86 s, Ar=792.
Figure 8	Evolution of oxygen concentration fields in the near wake of a confined bubble d_b=4.54± 0.15 mm for $10^o < \alpha < 60^o$ at different positions X' of 10, 30 and 60 mm at $Ar=800$.
Figure 9	Evolution of Oxygen concentration fields in the wake of confined bubbles of $4.54 < d_b < 10.94$ mm, $883< Ar <3221$, $396 <Re<2315$ under $\alpha= 30^o$ at the same $X' = 57$ mm.
Figure 10	Transferred mass m_{O2} (g) as function depending on inclination angle α for confined bubbles of equivalent diameters d_b=4.54 ± 0.15 mm and d_b=6.34 ± 0.15 mm at the same position X'=0.057 m.
Figure 11	Evolution of mass flux density $\varphi(X')$ as function of X' during sliding of a bubble having d_b=4.54±0.15 mm at Ar = 800 at different angles of inclination.
Figure 12	Evolution of liquid-side mass transfer coefficient (m/s) depending on inclination angle α for confined sliding bubbles of equivalent diameters d_b=4.54 ± 0.15 mm and d_b=6.34 ± 0.15 mm.
Figure 13	Scaling law for gas-liquid mass transfer around sliding bubble depending on inclination angle α.

References

[1] R. Clift, J.. Grace, M.. Weber, Bubbles, Drops, and Particles, Academic Press, 1978.

[2] F. Risso, Agitation, Mixing, and Transfers Induced by Bubbles, Annu. Rev. Fluid Mech. 50 (2018) 25–48. doi:10.1146/annurev-fluid-122316-045003.

[3] S. Haase, D.Y. Murzin, T. Salmi, Review on hydrodynamics and mass transfer in minichannel wall reactors with gas–liquid Taylor flow, Chem. Eng. Res. Des. 113 (2016) 304–329. doi:10.1016/j.cherd.2016.06.017.

[4] M.T. Kreutzer, F. Kapteijn, J.A. Moulijn, Shouldn ' t catalysts shape up ? Structured reactors in general and gas – liquid monolith reactors in particular, Catal. Today. 111 (2006) 111–118. doi:10.1016/j.cattod.2005.10.014.

[5] K.F. Jensen, Microreaction engineering — is small better?, Chem. Eng. Sci. 56 (2001) 293–303. doi:10.1016/S0009-2509(00)00230-X.

[6] M. Roudet, A.-M. Billet, S. Cazin, F. Risso, V. Roig, Experimental Investigation of Interfacial Mass Transfer Mechanisms for a Confined High-Reynolds-Number Bubble Rising in a Thin Gap, AIChE J. 00 (2016) 3–194. doi:10.1002/aic.

[7] M. Roudet, K. Loubiere, C. Gourdon, M. Cabassud, Hydrodynamic and mass transfer in inertial gas-liquid flow regimes through straight and meandering millimetric square channels, Chem. Eng. Sci. 66 (2011) 2974–2990. doi:10.1016/j.ces.2011.03.045.

[8] V. Roig, M. Roudet, F. Risso, A.M. Billet, Dynamics of a high-Reynolds-number bubble rising within a thin gap, J. Fluid Mech. 707 (2012) 444–466. doi:10.1017/jfm.2012.289.

[9] T. Maxworthy, Bubble rise under an inclined plate, J. Fluid Mech. 229 (1991) 659–674. doi:10.1017/S002211209100321X.

[10] T. Maxworthy, Bubble formation, motion and interaction in a Hele-Shaw cell, J. Fluid Mech.

173 (1986) 95–114. doi:10.1017/S002211208600109X.

[11] J. Timmermann, M. Hoffmann, M. Schlüter, Influence of Bubble Bouncing on Mass Transfer and Chemical Reaction, Chem. Eng. Technol. 39 (2016) 1955–1962. doi:10.1002/ceat.201600299.

[12] L. Yang, K. Loubière, N. Dietrich, C. Le Men, C. Gourdon, G. Hébrard, Local investigations on the gas-liquid mass transfer around Taylor bubbles flowing in a meandering millimetric square channel, Chem. Eng. Sci. 165 (2017) 192–203. doi:10.1016/j.ces.2017.03.007.

[13] A. Kherbeche, J. Milnes, M. Jimenez, N. Dietrich, G. Hébrard, B. Lekhlif, Multi-scale analysis of the influence of physicochemical parameters on the hydrodynamic and gas-liquid mass transfer in gas/liquid/solid reactors, Chem. Eng. Sci. 100 (2013) 515–528. doi:10.1016/j.ces.2013.06.025.

[14] E. Bouche, V. Roig, F. Risso, A.M. Billet, Homogeneous swarm of high-Reynolds-number bubbles rising within a thin gap. Part 2. Liquid dynamics, J. Fluid Mech. 758 (2014) 508–521. doi:10.1017/jfm.2014.544.

[15] K. Wongwailikhit, P. Warunyuwong, N. Chawaloes-Phonsiya, N. Dietrich, G. Hébrard, P. Pisut, Gas Sparger Orifice Sizes and Solid Particle Characteristics in a Bubble Column Relative Effect on Hydrodynamics and Mass Transfer, Chem. Eng. Technol. 41 (2018) 461–468. doi:10.1002/ceat.201700293.

[16] T. Maxworthy, The nonlinear growth of a gravitationally unstable interface in a hele shaw cell, J. Fluid Mech. 177 (1987) 207–232. doi:10.1017/S0022112087000922.

[17] A. Filella, P. Ern, V. Roig, Oscillatory motion and wake of a bubble rising in a thin-gap cell, J. Fluid Mech. 778 (2015) 60–88. doi:10.1017/jfm.2015.355.

[18] A.W.G. De Vries, Path and wake of a rising bubble, University of Twente, 2001. doi:ISBN 90 365 15262 Copyright.

[19] J. Magnaudet, I. Eames, The Motion of High-Reynolds-Number Bubbles in Inhomogeneous

Flos, Annu. Rev. Fluid Mech. 32 (2000) 659–708.

[20] H.W. Jia, P. Zhang, Mass transfer of a rising spherical bubble in the contaminated solution with chemical reaction and volume change, Int. J. Heat Mass Transf. 110 (2017) 43–57. doi:10.1016/j.ijheatmasstransfer.2017.02.095.

[21] A. Dani, P. Guiraud, A. Cockx, Local measurement of oxygen transfer around a single bubble by planar laser-induced fluorescence, Chem. Eng. Sci. 62 (2007) 7245–7252. doi:10.1016/j.ces.2007.08.047.

[22] M. Jimenez, N. Dietrich, G. Hébrard, Mass transfer in the wake of non-spherical air bubbles quantified by quenching of fluorescence, Chem. Eng. Sci. 100 (2013) 160–171. doi:10.1016/j.ces.2013.01.036.

[23] J. Francois, N. Dietrich, P. Guiraud, A. Cockx, Direct measurement of mass transfer around a single bubble by micro-PLIFI, Chem. Eng. Sci. 66 (2011) 3328–3338. doi:10.1016/j.ces.2011.01.049.

[24] M. Jimenez, N. Dietrich, G. Hebrard, a New Method for Measuring Diffusion Coefficient of Gases in Liquids By Plif, Mod. Phys. Lett. B. 26 (2012) 1150034. doi:10.1142/S0217984911500345.

[25] M. Roudet, Hydrodynamique et transfert de masse autour d’une bulle confinée entre deux plaques, University of Toulouse, 2008.

[26] R. O’Reilly Meehan, B. Donnelly, K. Nolan, T. Persoons, D.B. Murray, Flow structures and dynamics in the wakes of sliding bubbles, Int. J. Multiph. Flow. 84 (2016) 145–154. doi:10.1016/j.ijmultiphaseflow.2016.03.010.

[27] B. Donnelly, R. O’Reilly Meehan, K. Nolan, D.B. Murray, The dynamics of sliding air bubbles and the effects on surface heat transfer, Int. J. Heat Mass Transf. 91 (2015) 532–542. doi:10.1016/j.ijheatmasstransfer.2015.07.133.

[28] R. O’Reilly Meehan, K. Grennan, I. Davis, K. Nolan, D.B. Murray, Visualization of the wake

behind a sliding bubble, Phys. Rev. Fluids. 2 (2017) 104303. doi:10.1103/PhysRevFluids.2.104303.

[29] A. Zaruba, D. Lucas, H.M. Prasser, T. Höhne, Bubble-wall interactions in a vertical gas-liquid flow: Bouncing, sliding and bubble deformations, Chem. Eng. Sci. 62 (2007) 1591–1605. doi:10.1016/j.ces.2006.11.044.

[30] B. Donnelly, A.J. Robinson, Y.M.C. Delauré, D.B. Murray, Sliding bubble dynamics and the effects on surface heat transfer, J. Phys. Conf. Ser. 395 (2012) 012180. doi:10.1088/1742-6596/395/1/012180.

[31] H. Jeong, H. Park, Near-wall rising behaviour of a deformable bubble at high Reynolds number, J. Fluid Mech. 771 (2015) 564–594. doi:10.1017/jfm.2015.191.

[32] J. Xu, B. Chen, Y. Huang, X. Yan, D. Yuan, Experimental visualization of sliding bubble dynamics in a vertical narrow rectangular channel, Nucl. Eng. Des. 261 (2013) 156–164. doi:10.1016/j.nucengdes.2013.02.055.

[33] L.-S. Fan, K. Tsuchiya, Bubble Wake Dynamics in Liquids and Liquid-Solid Suspensions, Butterworth-Heinemann, 1990.

[34] R. Higbie, The rate of absorption of a pure gas into a still liquid during short periods of exposure, Transctions Am. Inst. Chem. Eng. 29 (1935) 146–148.

[35] P.V. Danckwerts, Significance of Liquid-Film Coefficients in Gas Absorption, Ind. Eng. Chem. Res. 43 (1951) 1460–1467. doi:10.1021/ie50498a055.

[36] N. Dietrich, K. Loubiere, M. Jimenez, G. Hebrard, C. Gourdon, A new direct technique for visualizing and measuring gas-liquid mass transfer around bubbles moving in a straight millimetric square channel, Chem. Eng. Sci. 100 (2013) 172–182. doi:10.1016/j.ces.2013.03.041.

[37] P. Kováts, D. Pohl, D. Thévenin, K. Zähringer, Optical determination of oxygen mass transfer in a helically-coiled pipe compared to a straight horizontal tube, Chem. Eng. Sci. 190 (2018)

273–285. doi:10.1016/j.ces.2018.06.029.

[38] N. Dietrich, G. Hebrard, Visualisation of gas-liquid mass transfer around a rising bubble in a quiescent liquid using an oxygen sensitive dye, Heat Mass Transf. (2018). doi: 10.1007/s00231-018-2297-3.

[39] L. Yang, N. Dietrich, G. Hébrard, K. Loubière, C. Gourdon, Optical methods to investigate the enhancement factor of an oxygen-sensitive colorimetric reaction using microreactors, AIChE J. 63 (2017) 2272–2284. doi:10.1002/aic.15547.

[40] D. Colombet, D. Legendre, F. Risso, A. Cockx, P. Guiraud, Dynamics and mass transfer of rising bubbles in a homogenous swarm at large gas volume fraction, J. Fluid Mech. 763 (2015) 254–285. doi:10.1017/jfm.2014.672.